

## Article

# An Electrospun Porous $\text{CuBi}_2\text{O}_4$ Nanofiber Photocathode for Efficient Solar Water Splitting

Xiuhua Yuan <sup>1</sup>, Yeling Liu <sup>2</sup>, Hui Yuan <sup>2</sup>, Bingxin Liu <sup>2</sup>, Tianyu Guo <sup>3</sup>, Huawei Zhou <sup>2</sup> and Xia Li <sup>2,\*</sup> 

<sup>1</sup> School of Mechanical and Automotive Engineering, Liaocheng University, Liaocheng 252000, China; yuanxiuhua@lcu.edu.cn

<sup>2</sup> Department of Chemistry, Liaocheng University, Liaocheng 252000, China; 1910120301@stu.lcu.edu.cn (Y.L.); 2010120316@stu.lcu.edu.cn (H.Y.); 2018204269@stu.lcu.edu.cn (B.L.); zhouhuawei@lcu.edu.cn (H.Z.)

<sup>3</sup> Department of Art and Science, University of Vermont, Burlington, VT 05405, USA; tguo18@jh.edu

\* Correspondence: lixia@lcu.edu.cn

**Abstract:** While the  $\text{CuBi}_2\text{O}_4$ -based photocathode has emerged as an ideal candidate for photoelectrochemical water splitting, it is still far from its theoretical values due to poor charge carrier transport, poor electron–hole separation, and instability caused by self-photoelectric-corrosion with electrolytes. Establishing synthesis methods to produce a  $\text{CuBi}_2\text{O}_4$  photocathode with sufficient cocatalyst sites would be highly beneficial for water splitting. Here, the platinum-enriched porous  $\text{CuBi}_2\text{O}_4$  nanofiber ( $\text{CuBi}_2\text{O}_4/\text{Pt}$ ) with uniform coverage and high surface area was prepared as a photocathode through an electrospinning and electrodeposition process for water splitting. The prepared photocathode material was composed of a  $\text{CuBi}_2\text{O}_4$  nanofiber array, which has a freestanding porous structure, and the Pt nanoparticle is firmly embedded on the rough surface. The highly porous nanofiber structures allow the cocatalyst (Pt) better alignment on the surface of  $\text{CuBi}_2\text{O}_4$ , which can effectively suppress the electron–hole recombination at the electrolyte interface. The as-fabricated  $\text{CuBi}_2\text{O}_4$  nanofiber has a tetragonal crystal structure, and its band gap was determined to be 1.8 eV. The self-supporting porous structure and electrocatalytic activity of Pt can effectively promote the separation of electron–hole pairs, thus obtaining high photocurrent density (0.21 mA/cm<sup>2</sup> at 0.6 V vs. RHE) and incident photon-to-current conversion efficiency (IPCE, 4% at 380 nm). This work shows a new view for integrating an amount of Pt nanoparticles with  $\text{CuBi}_2\text{O}_4$  nanofibers and demonstrates the synergistic effect of cocatalysts for future solar water splitting.

**Keywords:** electrospinning;  $\text{CuBi}_2\text{O}_4$  nanofiber; photocathode; water splitting



**Citation:** Yuan, X.; Liu, Y.; Yuan, H.; Liu, B.; Guo, T.; Zhou, H.; Li, X. An Electrospun Porous  $\text{CuBi}_2\text{O}_4$  Nanofiber Photocathode for Efficient Solar Water Splitting. *Polymers* **2021**, *13*, 3341. <https://doi.org/10.3390/polym13193341>

Academic Editor: Andrea Ehrmann

Received: 28 July 2021

Accepted: 12 August 2021

Published: 29 September 2021

**Publisher's Note:** MDPI stays neutral with regard to jurisdictional claims in published maps and institutional affiliations.



**Copyright:** © 2021 by the authors. Licensee MDPI, Basel, Switzerland. This article is an open access article distributed under the terms and conditions of the Creative Commons Attribution (CC BY) license (<https://creativecommons.org/licenses/by/4.0/>).

## 1. Introduction

It is imperative to find sustainable alternative energy to cope with humankind's energy source crisis [1,2]. Photoelectrochemical water splitting for hydrogen under solar irradiation is seen as the ultimate way to solve the energy crisis [3–6]. A critical challenge for photoelectrochemical water splitting is the low conversion efficiency suffering from poor charge carrier transport and poor electron–hole separation. In order to improve the efficiency of water splitting, it is necessary to explore a new type of photoelectric material with the best band gap and photocurrent starting potential [7–10]. In this regard, copper-based oxides-based photocathodes with natural p-type conductivity are a very good choice for their high photocurrents [10–12]. Nevertheless, the Cu 3d character in the conduction band of  $\text{Cu}_2\text{O}$  will lead to photoelectron-induced self-reduction and poor operational stability [10,11]. Therefore, it is urgent to develop a new type of copper-based metal oxide photocathode, so that the  $\text{Cu}_2\text{O}$  conduction band is sheared, and the photogenerated electrons are directed to the redox stable metal orbitals.

Substantial studies have revealed  $\text{CuBi}_2\text{O}_4$ , a multinary p-type metal oxide semiconductor that alloys  $\text{Cu}_2\text{O}$  with Bi oxide, and its ternary alloy structure allows the photogenerated electrons to be directed toward redox stable metal orbitals [12]. Such  $\text{CuBi}_2\text{O}_4$

possesses a sufficiently narrow direct bandgap and exceptionally positive photocurrent onset potential ( $>1.0$  V vs. RHE), thus improving solar energy utilization [13–16]. For example, a powder-type  $\text{CuBi}_2\text{O}_4$  photocatalyst can be realized by hypoxic calcination [17], hydrothermal synthesis [18], and the sol–gel method [19]. Although the photocathode prepared by powder-type  $\text{CuBi}_2\text{O}_4$  has various desirable properties, it has not achieved a high photoelectric conversion efficiency. Photocathode corrosion often occurs during oxygen reduction due to the poor transport property of the carrier ( $\sim 1.2 \times 10^{-3} \text{ cm}^2/\text{Vs}$ ) [14]. Therefore, substantial improvements in activity and stability are greatly needed.

Recently, the coupling of film-type  $\text{CuBi}_2\text{O}_4$  with different noble metal decorative materials has attracted widespread attention due to its synergistic effect, which can increase photoelectrochemical activity [20]. Such  $\text{CuBi}_2\text{O}_4$  film can be realized by hydrothermal synthesis, chemical bath deposition [21], and a template-directed method [22]. For example, Xu et al. demonstrated Au coating film-type  $\text{CuBi}_2\text{O}_4$  photocathodes with high photoelectrochemical activity through coupling p-type doping with Au and gradient Cu-vacancy doping [23,24]. Cao et al. fabricated  $\text{CuBi}_2\text{O}_4$  film decorated with Pt nanoparticles using atomic layer deposition and indicated an attractive p-type material in water splitting without concern for the corrosion problem in aqueous electrolytes [16]. Park et al. reported a  $\text{CuO}|\text{CuBi}_2\text{O}_4$  film coated with Pt layers for water splitting and showed more than double the photoactivity compared to the corresponding monolayer photocathode [25]. The photoelectrochemical properties of such polycrystalline thin films can vary significantly, which mainly depend on their morphological details (such as uniform coverage, surface area, and the size and number of cocatalysts) [26–29]. Although the thin-film  $\text{CuBi}_2\text{O}_4$  photocathode system has a high application efficiency, its application scope is limited, especially in dense thin films, which often suffer from the recombination of electron-hole pairs [20]. Therefore, designing a simple and effective synthesis method to obtain a stable extensible film-type  $\text{CuBi}_2\text{O}_4$  photoelectrode with sufficient active sites will be very conducive to improving water splitting.

Electrospinning provides a simple and scalable synthesis method to fabricate one-dimensional nanomaterial [30] and has been proven particularly useful in the field of photocatalysis [31–33]. While electrospinning has been used to fabricate  $\text{CuO}$  nanofibers [34] and  $\text{BiVO}_4$  nanotubes [35] for solar water splitting, no studies have been reported on fabricating  $\text{CuBi}_2\text{O}_4$  nanofibers. Here, the novel platinum-enriched porous  $\text{CuBi}_2\text{O}_4$  nanofiber ( $\text{CuBi}_2\text{O}_4/\text{Pt}$ ) with uniform coverage and high surface area was prepared as a photocathode through an electrospinning and electrodeposition process for efficient water splitting. The prepared photocathode material was composed of a  $\text{CuBi}_2\text{O}_4$  nanofiber array, which has a freestanding porous structure, and the Pt nanoparticle was firmly embedded on the rough surface. The porous nanofiber structure makes the cocatalyst (Pt) better arranged on the  $\text{CuBi}_2\text{O}_4$  surface, which effectively prevents the electron–hole pair recombination at the electrolyte interface. The as-fabricated  $\text{CuBi}_2\text{O}_4$  nanofiber has a tetragonal crystal structure, and its band gap was determined to be 1.8 eV. The self-supporting porous structure and cocatalytic activity of Pt can effectively promote the separation of electron–hole pairs, resulting in high photocurrent density ( $0.21 \text{ mA}/\text{cm}^2$  at 0.6 V vs. RHE) and IPCE (4% at 380 nm). This study provides a new idea for the integration of Pt nanoparticles and  $\text{CuBi}_2\text{O}_4$  nanofibers and provides a synergistic catalyst for future solar water splitting.

## 2. Materials and Methods

The  $\text{CuBi}_2\text{O}_4/\text{Pt}$  nanofiber film was synthesized via a three-step process: electrospinning, annealing, and deposition, which is shown in Figure 1.

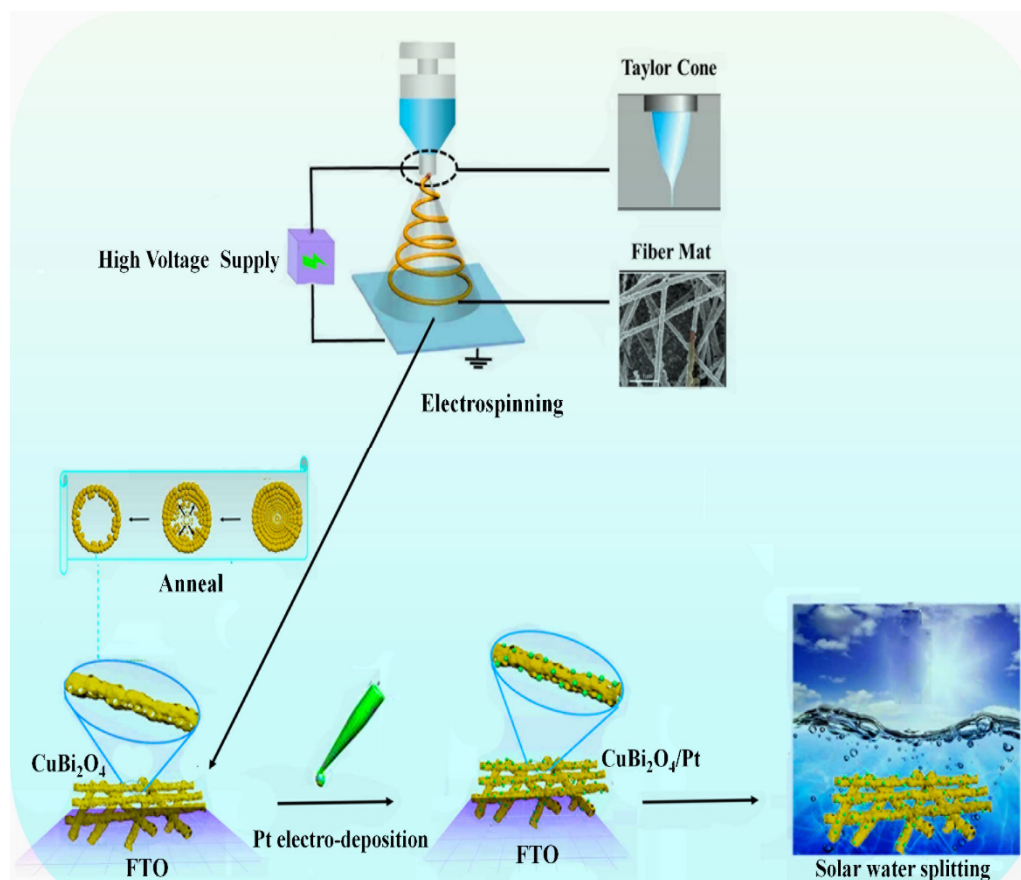


**Figure 1.** Schematic illustration of the CuBi<sub>2</sub>O<sub>4</sub>/Pt nanofiber fabrication process.

### 2.1. Materials

The polyvinylpyrrolidone (PVP, K90, Mw = 1,300,000) and chloroplatinic acid (H<sub>2</sub>PtCl<sub>6</sub>·6H<sub>2</sub>O) were from Aladdin, Shanghai, China. The bismuth nitrate pentahydrate (Bi(NO<sub>3</sub>)<sub>3</sub>·5H<sub>2</sub>O), cupric nitrate (Cu(NO<sub>3</sub>)<sub>2</sub>·3H<sub>2</sub>O), N,N-Dimethylformamide (DMF), and acetic acid (CH<sub>3</sub>COOH) were obtained from J&K Chemical Ltd., B, Beijing, China. All materials were of analytical grade without further purification.

### 2.2. Preparation of Porous CuBi<sub>2</sub>O<sub>4</sub>/Pt Nanofiber Film

The synthesis of the precursor solution followed two steps: first of all, the Bi(NO<sub>3</sub>)<sub>3</sub>·5H<sub>2</sub>O and Cu(NO<sub>3</sub>)<sub>2</sub>·3H<sub>2</sub>O were added to a mixture of acetic acid and DMF and stirred 1 h to ensure dissolution; then the PVP was added to the above mixture and stirred 10 h to form the homogeneous precursor (Figure S1a, Supplementary Materials). The electrospinning was carried out with a self-made apparatus [35], which was composed of a plastic syringe, a high voltage supply, and a plate collector. The homogeneous precursor was injected into the syringe with a stainless steel needle (diameter = 0.5 mm). The FTO glass (OPV-FTO-22-07, 2.5 × 3 cm<sup>2</sup>) was pasted on the counter plate to collect nanofibers. The electrospinning was performed at a distance of 20 cm between the tip of the steel needle and the plate collector, at a high voltage of 20 kV, at an injection rate of 0.1 mL/h, and with an air humidity of 40%. After electrospinning for 25 min, the films collected on the FTO glass (Figure S1b, Supplementary Materials) were dried at 100 °C for 5 h. Based on the thermogravimetry curve (Figure S2, Supplementary Materials), the nanofiber film on FTO was annealed at 520 °C for 1 h and naturally cooled down to ambient temperature. Finally, the photocathode of CuBi<sub>2</sub>O<sub>4</sub> nanofibers (Figure S1c, Supplementary Materials) was successfully obtained.

The Pt nanoparticles were loaded onto the CuBi<sub>2</sub>O<sub>4</sub> nanofibers by electrodeposition, as the PtCl<sub>6</sub><sup>2+</sup> can be reduced to Pt nanoparticles at low potential. A three-electrode

system was employed with an as-prepared nanofiber on FTO glass (working electrode), an Ag/AgCl reference electrode, and a platinum counter electrode. The electrolyte was 0.1 mM  $\text{H}_2\text{PtCl}_6 \cdot 6\text{H}_2\text{O}$  in 0.1 M potassium borate buffer (pH = 7.0). The electrodeposition was carried out using an electrochemical workstation (Zahner Zennium) at  $-0.20$  V versus Ag/AgCl for 1 min.

### 2.3. Physical Characterization

In order to investigate the nanofiber, its morphology was measured by a scanning electron microscope (SEM, Zeiss Merlin), an energy-dispersive X-ray spectroscopy (EDS), and a transmission electron microscope (TEM, JEM-2100). Its chemical element and crystallinity were characterized by X-ray photoelectron spectroscopy (XPS, ESCALAB Xi +) and X-ray diffraction (XRD, Bruker Smart-1000CCD diffractometer), respectively. The surface area of the  $\text{CuBi}_2\text{O}_4$  nanofiber was measured by the Brunauer–Emmett–Teller (BET, Micromeritics ASAP2460, Norcross, GA, USA). The UV-visible diffuse reflectance spectrum was characterized by a UV-vis spectrophotometer (PE lambda 750) with an integrated sphere attachment.

The photocatalytic  $\text{H}_2$  was carried out using the CEL-PAEM-D8 photocatalytic activity evaluation system, which consisted of a gas chromatograph (Agilent Technologies GC-7890B) and a 300 W Xe lamp (MicroSolar 300, Perfect Light). The circulation water of  $25^\circ\text{C}$  was applied to maintain the reaction temperature of the solution. The photoelectrochemical experiments on the  $\text{CuBi}_2\text{O}_4/\text{Pt}$  nanofiber photocathode were performed on the Zahner electrochemical workstation in a three-electrode cell (the  $\text{CuBi}_2\text{O}_4/\text{Pt}$  nanofibers on FTO, Ag/AgCl reference electrode, and a platinum counter electrode, respectively). For photocurrent measurements, the electrolyte was 0.2 M PBS (pH 7.0). The Xe lamp (CEL-HXF300-T3, P =  $100\text{ mW}/\text{cm}^2$ , AM1.5) was used as the illumination source. The light intensity was adjusted by a calibrated photodetector. For incident photon-to-current efficiency (IPCE) measurements, the CIMPS TLS03 model (Zahner tunable light source system) was employed for monochromatic light excitation. The chopped photocurrent–voltammetry measurement was carried out with a scan speed of  $10\text{ mV}/\text{s}$  and a chopped light time of 8 s.

## 3. Results

### 3.1. Morphology and Structure of Nanofibers

As indicated in Figure S1b (Supplementary Materials), a typical digital photo of the as-spun film before annealing shows white. After high-temperature annealing, the photocathode shown in Figure S1c (Supplementary Materials) changes to a transparent yellow, which is similar to the spray  $\text{CuBi}_2\text{O}_4$  photocathode. The morphology of the  $\text{CuBi}_2\text{O}_4$  nanofibers was evaluated by TEM and SEM measurements. As shown in Figure 2a, the randomly oriented nanofibers inherited the one-dimensional structure, and the nonwoven film, which was composed of nanofibers, showed typically interconnected flyover-like network form. The high-magnification image of Figure 2b shows these nanofibers possess a porous fiber structure, which has sufficient surface active sites for photocatalytic reaction. As shown in Figure S3 (Supplementary Materials), the average diameter of the porous nanofiber was 225 nanometers, and its length was up to several dozen micrometers. Under low magnification, Figure 2c reveals one-dimensional morphology, and numerous connective nanoparticles make up the products, similar to the SEM results. The distance between adjacent lattice planes was measured to be 0.31 nm, which belongs to the crystal plane (211) of the  $\text{CuBi}_2\text{O}_4$  tetragonal phase (JCPDS 01-080-0996). Figure 2e shows the elemental mapping of the  $\text{CuBi}_2\text{O}_4$  nanofiber after depositing Pt. It can be seen that the Bi, Cu, and O elements were uniformly distributed inside the nanofiber. In addition, the Pt element was uniformly distributed on the surface of the nanofiber.

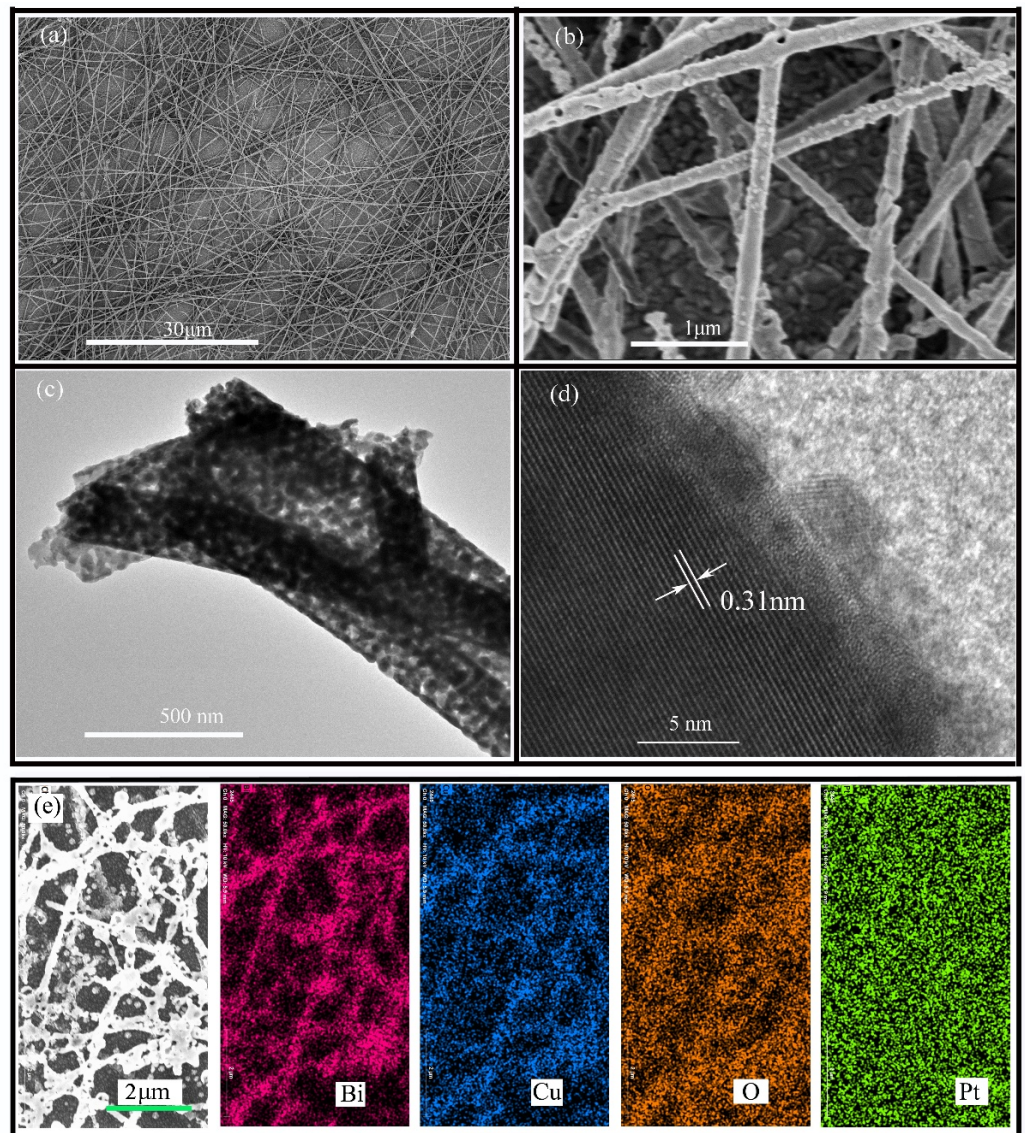


**Figure 2.** The  $\text{CuBi}_2\text{O}_4$  nanofibers' (a,b) SEM images and (c,d) TEM images; (e) the elemental mapping after depositing Pt.

As shown in Figure 3a, the diffraction peaks in  $20.9^\circ$ ,  $28.1^\circ$ ,  $33.5^\circ$ , and  $46.7^\circ$  corresponded to the crystal planes (200), (211), (310), and (411) of the tetragonal  $\text{CuBi}_2\text{O}_4$ , respectively (JCPDS 01-080-0996). The  $\text{SnO}_2$  phase of FTO glass was also marked on the same figure with an orange line. No other diffraction peak was found in the XRD pattern, which confirmed the high crystalline and phase purity of  $\text{CuBi}_2\text{O}_4$  after annealing. Detailed information about the surface element composition as well as the chemical state can be obtained by XPS. The survey scan spectrum (Figure 3b) revealed that these nanofibers were composed of Cu, Bi, and O elements. As shown in the high-resolution XPS spectra (Figure 3c–e), two main asymmetric peaks at 159.0 eV and 164.7 eV were attributed to  $\text{Bi}4f_{7/2}$  and  $\text{Bi}4f_{5/2}$ , corresponding to the oxidation state of  $\text{Bi}^{3+}$ . Then, the peaks at 954.0 and 934.4 eV were attributed to Cu 2p $_{1/2}$  and Cu 2p $_{3/2}$ . Together with a satellite peak at 942.0 eV, the copper mainly existed in the form of  $\text{Cu}^{2+}$ . Besides, the asymmetrical O1s peak (Figure 3e) ranging from 527 eV to 535 eV was fitted into two peaks at 529.4 and 531.0 eV, which were attributed to Cu–O and Sn–O ( $\text{SnO}_2$  phase of FTO glass) bonds, respectively. Together, both the XRD and XPS results confirmed that these nanofibers were highly crystallized.

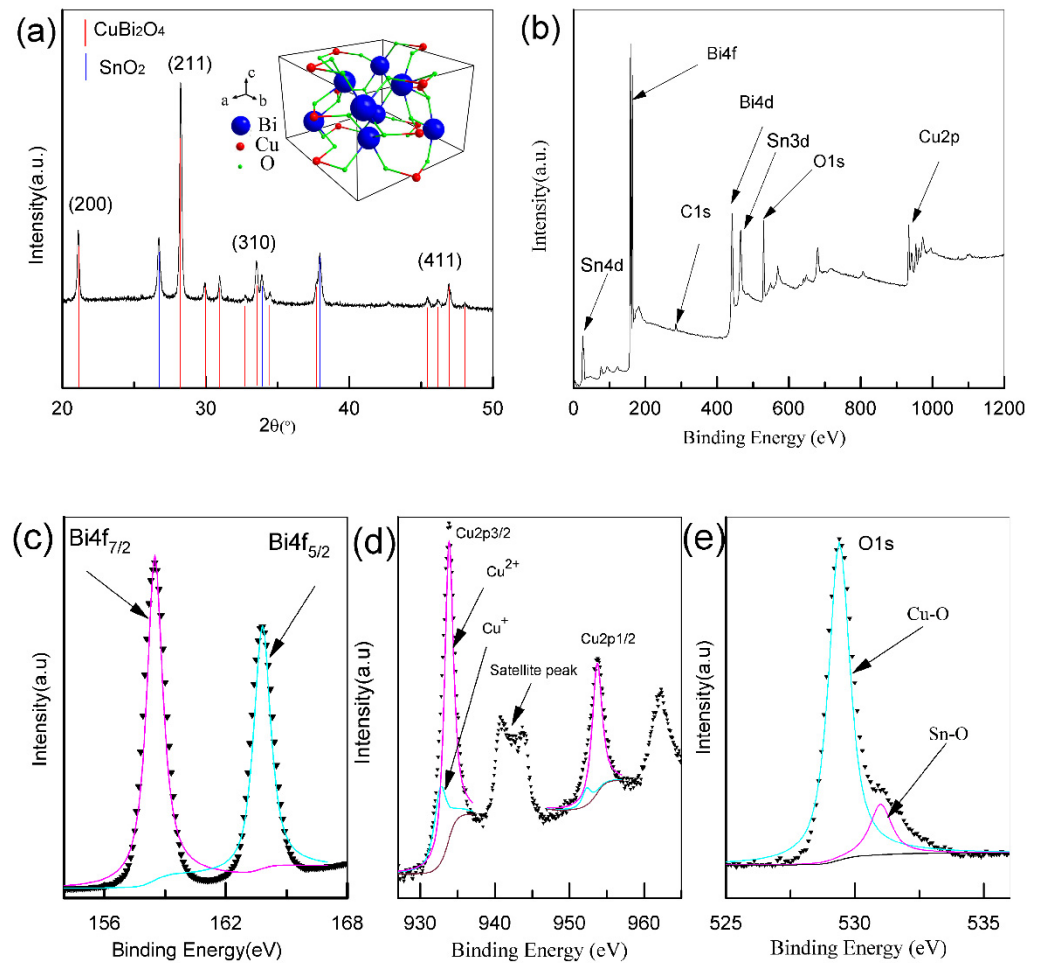


**Figure 3.** XRD pattern (a); XPS spectrum (b); high-resolution XPS spectra for (c) Bi4f; (d) Cu2p; and (e) O1s.

As indicated in Figure 4a, the  $\text{CuBi}_2\text{O}_4$  nanofibers exhibited strong UV-vis absorbance in both the ultraviolet and visible light regions, and their absorption cutoff wavelength was about 650 nm. By employing the linear part of  $(\alpha h\nu)^2$  vs.  $h\nu$ , the band gap was calculated to be 1.8 eV, which is similar to that reported in other studies (1.74 eV) [17]. From the nitrogen adsorption and desorption isotherms of  $\text{CuBi}_2\text{O}_4$  nanofibers (Figure 4b), the specific surface area of the  $\text{CuBi}_2\text{O}_4$  nanofibers was calculated to be  $20.5 \text{ m}^2\text{g}^{-1}$  using the Brunauer–Emmet–Teller model, which was larger than the value ( $14 \text{ m}^2\text{g}^{-1}$ ) of nanoparticles reported in other research [36].

### 3.2. Photoelectrochemical Performance

To investigate the photoelectrochemical activity of the  $\text{CuBi}_2\text{O}_4$  photocathode, the photocurrent–voltammetry measurement under AM 1.5 was performed. As shown in Figure 5a, the photocurrent started to appear at the initial potential of 1.0 V vs. RHE, increased rapidly when the lamp was turned on, and decreased when the lamp was turned off, indicating that the photocurrent was generated under light irradiation. Interestingly, the instantaneous photocurrent overshoot could also be observed when the lamp was switched on/off, which indicates that electrons accumulate in the space charge layer and reverse recombination occurs between electrons and holes. Moreover, the chopped photocurrent for the  $\text{CuBi}_2\text{O}_4/\text{Pt}$  nanofibers showed little cathodic transient spikes, which presumably were caused by surface recombination. Figure 5b indicates the photocurrent–voltage (J–V) curves under AM 1.5 irradiation. The photocurrent of  $\text{CuBi}_2\text{O}_4$  nanofibers rose slowly when decreasing the potential, and yielded  $-0.12 \text{ mA/cm}^2$  at 0.6 V vs. RHE.

On the contrary, after depositing the Pt nanoparticles, their photocurrent rose quickly when decreasing the potential and yielded  $-0.21 \text{ mA/cm}^2$  at  $0.6 \text{ V}$  vs. RHE. Remarkably, the photocurrent of  $\text{CuBi}_2\text{O}_4/\text{Pt}$  nanofibers was about 75% higher than that of the pristine nanofibers. Then, the IPCE measurement by the tunable light source TLS03 model at  $0.6 \text{ V}$  vs. RHE was performed. As indicated in Figure 5c, with the increase in illuminant wavelength, the IPCE values gradually decreased to zero at  $650 \text{ nm}$  ( $1.8 \text{ eV}$ ), which was consistent with its band gap energy. Significantly, compared to those of pristine nanofibers (1.8% at  $380 \text{ nm}$ ), the as-prepared  $\text{CuBi}_2\text{O}_4/\text{Pt}$  nanofibers showed a higher IPCE reaching up to 4% at  $380 \text{ nm}$ . As shown in Table S1, the nanofibers decorated with Pt exhibit higher photoelectrochemical performance (the value of photocurrent and IPCE) than that of  $\text{CuBi}_2\text{O}_4$  nanofilm ( $0.15 \text{ mA/cm}^2$  at  $0.6 \text{ V}$  vs. RHE) [21]. Nevertheless, the gradient self-doping nanofilm ( $0.50 \text{ mA/cm}^2$  at  $0.6 \text{ V}$  vs. RHE) showed higher photoelectrochemical performance than that of the as-prepared  $\text{CuBi}_2\text{O}_4/\text{Pt}$  nanofiber due to its internal electric field promoting charge separation. [19].

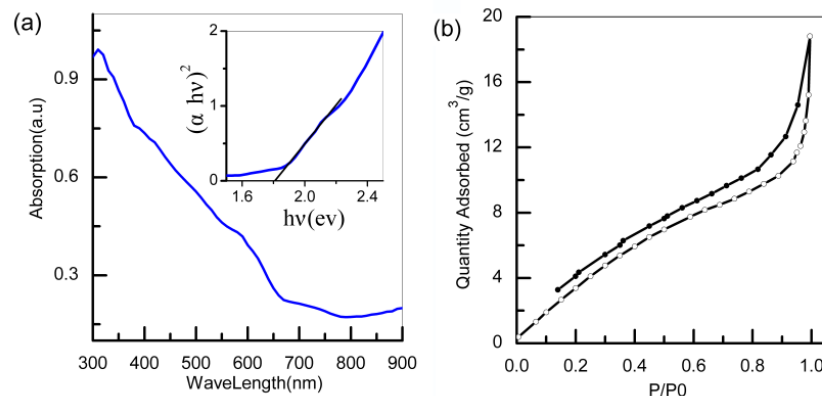


**Figure 4.** UV-vis absorption spectra (a);  $\text{N}_2$  adsorption–desorption isotherms (b) of  $\text{CuBi}_2\text{O}_4$  nanofibers.

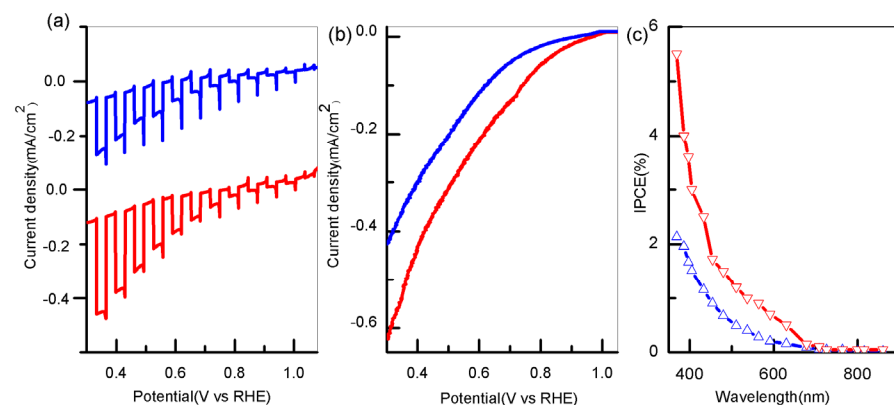


**Figure 5.** (a) Chopped photocurrent vs. voltage curves; (b) photocurrent vs. voltage (J–V) curves; (c) IPCE spectrum (blue and red lines represent before and after depositing Pt).

As indicated in Figure 6a, the photocurrent of the  $\text{CuBi}_2\text{O}_4/\text{Pt}$  nanofibers photocathode decreased obviously with the increase in time at  $0.6 \text{ V}$  versus RHE and decreased by nearly 40% after 25 min illumination. Nevertheless, the photostability of the  $\text{CuBi}_2\text{O}_4/\text{Pt}$  nanofibers photocathode was better than that of the pure  $\text{Cu}_2\text{O}$  [37] and  $\text{CuO}$  (52% reduction of photocurrent after 25 min illumination [38]) photocathode. The photocurrent decay was mainly caused by photocorrosion, and a similar phenomenon also appeared at the  $\text{CuBi}_2\text{O}_4$  photocathode consisting of open windows and struts [14]. The photocatalytic

H<sub>2</sub> production of the fabricated nanofibers was measured by the gas chromatography-mass spectrometer (GC-7890B). As shown in Figure 6b, CuBi<sub>2</sub>O<sub>4</sub>/Pt nanofibers exhibited higher photocatalytic performance (380 μmol/(g·h)) compared to the CuBi<sub>2</sub>O<sub>4</sub> nanofibers (290 μmol/(g·h)). Nonetheless, its photocatalytic performance was much lower than that of Pt/TiO<sub>2</sub> nanosheet with exposed (001) facet (8500 μmol/(g·h), [39]). The main reason was that although the one-dimensional nanostructure could reduce the recombination of photogenerated electron-hole pairs, some electron-hole pairs still recombined due to the poor transport property of the carrier ( $\sim 1.2 \times 10^{-3} \text{ cm}^2/\text{Vs}$ , [14]). In addition, the photocatalytic activity of these nanofibers slightly decreased with time due to photocorrosion. The instability of CuBi<sub>2</sub>O<sub>4</sub> nanofibers presents a major challenge for solar water splitting, and protection layers using atomic layer deposition were essential in order to use them as a practical photocathode.

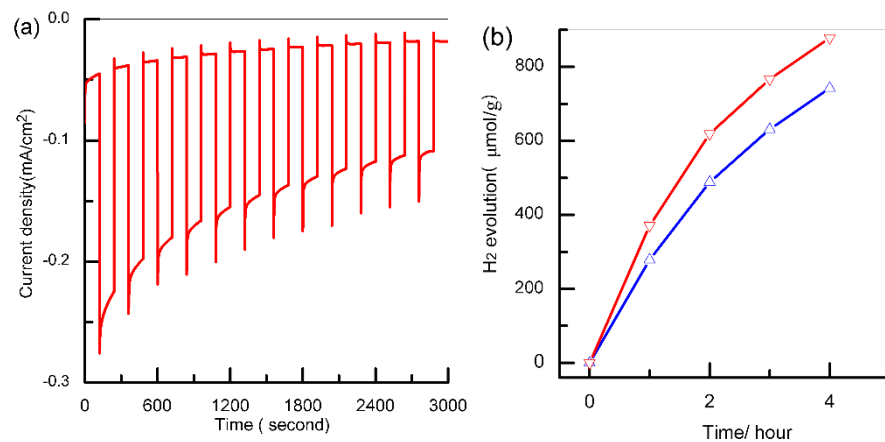


**Figure 6.** (a) Chopped photocurrent vs. time curve at 0.6 V vs. RHE; (b) the time courses of H<sub>2</sub> evolution under AM 1.5 with methanol as a sacrificial reagent (blue and red lines represent before and after depositing Pt).

Based on the above analysis of experimental data, the transfer process of the electron-hole pair in the photocathode was shown in Figure 7. Under light illumination, the CuBi<sub>2</sub>O<sub>4</sub> nanofibers could absorb photons and excite the valence electron to the conduction band. Then the photogenerated electron moved to the interface between the photocathode and the electrolyte due to the downward band bending and injected into the electrolyte to take part in the reduction reaction of hydrogen, which was similar to the charge transfer of BiVO<sub>4</sub> anode [35]. As shown in Figure 5a, there are amounts of recombination of electron-hole pairs during the water splitting reaction. The photoelectrochemical test demonstrates that the CuBi<sub>2</sub>O<sub>4</sub>/Pt nanofibers show better photocatalytic activity. The main reasons are as follows: Firstly, nanofibers have a large specific surface area and porous structure, which maintain good contact with electrolytes and enrich the active sites. Moreover, the nanofibers, possessing a one-dimensional structure, can also shorten the length of hole diffusing to the FTO substrate and decrease the recombination of the electron-hole pair. In addition, the Pt cocatalyst can also efficiently extract a photogenerated electron from the space charge layer. Therefore, more electrons can be transferred into electrolytes to take part in the reduction reaction of hydrogen, and the electron-hole recombination is significantly hindered. In summary, the main reasons for the enhanced photoelectrochemical performance of CuBi<sub>2</sub>O<sub>4</sub>/Pt nanofiber photocathode are porous nanofibers and cocatalysts.

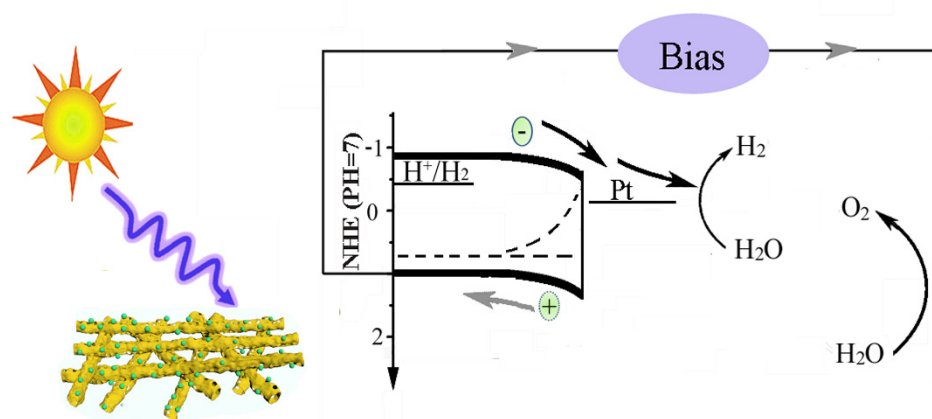


**Figure 7.** The transport process of electron–hole pairs.

#### 4. Conclusions

In summary, the platinum-enriched porous  $\text{CuBi}_2\text{O}_4$  nanofibers ( $\text{CuBi}_2\text{O}_4/\text{Pt}$ ) with uniform coverage and high surface area were prepared as a photocathode through an electrospinning and electrodeposition process for improving the photoelectrochemical water splitting. The  $\text{CuBi}_2\text{O}_4$  nanofibers showed an average diameter of 225 nanometers, and lengths up to several dozens of micrometers. The porous nanofiber structures allow the cocatalyst (Pt) to have better alignment on the surface of  $\text{CuBi}_2\text{O}_4$ , which can effectively hinder the electron–hole recombination at the electrolyte interface. These nanofibers have a tetragonal crystal structure, and their band gap was determined to be 1.8 eV. After depositing Pt nanoparticles, their photocurrent density was  $0.21 \text{ mA/cm}^2$  at 0.6 V vs. RHE under AM 1.5 illumination, and the IPCE was 4% at 380 nm. The enhanced photoelectrochemical ability was mainly attributed to the porous nanofibers, large specific surface area, and the cocatalytic activity of Pt nanoparticles. This work shows a new view for integrating an amount of Pt nanoparticles with  $\text{CuBi}_2\text{O}_4$  nanofibers, indicating the synergistic effect of cocatalysts for efficient storage of solar energy into hydrogen.

**Supplementary Materials:** The following are available online at <https://www.mdpi.com/article/10.3390/polym13193341/s1>, Figure S1: Digital micrograph of (a) solution precursor, (b) PVP- $\text{CuBi}_2\text{O}_4$  nanofiber mat before annealing and (c)  $\text{CuBi}_2\text{O}_4$  nanofiber mat after annealing; Figure S2: TG-DSC curve of the crystallization of  $\text{CuBi}_2\text{O}_4$  nanofiber; Figure S3:  $\text{CuBi}_2\text{O}_4$  nanofiber (a) SEM, (b) corresponding diameter distribution; Table S1: Comparison of photocurrent data reported in the literature with the photocurrent value obtained in the present study.

**Author Contributions:** Conceptualization, X.Y.; methodology, Y.L.; formal analysis, H.Y.; investigation, T.G.; resources; H.Z., data curation, B.L.; writing—original draft preparation, X.Y.; writing—review and editing; X.L., funding acquisition. All authors have read and agreed to the published version of the manuscript.

**Funding:** This work was supported by the Natural Science Foundation of Shandong Province (No. ZR2019MB068), and A Project of Shandong Province Higher Educational Science and Technology Program (No. KJ2018BZC043).

**Institutional Review Board Statement:** Not applicable.

**Informed Consent Statement:** Not applicable.

**Data Availability Statement:** The data presented in this study are available upon request from the corresponding author.

**Conflicts of Interest:** The authors declare no conflict of interest.

## References

1. Cook, T.R.; Dogutan, D.K.; Reece, S.Y.; Surendranath, Y.; Teets, T.; Nocera, D. Solar energy supply and storage for the legacy and non legacy worlds. *Chem. Rev.* **2010**, *110*, 6474–6502. [[CrossRef](#)]
2. Chu, S.; Majumdar, A. Opportunities and challenges for a sustainable energy future. *Nature* **2012**, *488*, 294–303. [[CrossRef](#)]
3. Roger, I.; Shipman, M.A.; Symes, M.D. Earth-abundant catalysts for electrochemical and photoelectrochemical water splitting. *Nat. Rev. Chem.* **2017**, *1*, 1–13. [[CrossRef](#)]
4. Yao, T.; An, X.; Han, H.; Chen, J.Q.; Li, C. Photoelectrocatalytic materials for solar water splitting. *Adv. Energy Mater.* **2018**, *8*, 1800210–1800237. [[CrossRef](#)]
5. Xu, P.; Mccool, N.S.; Mallouk, T.E. Water splitting dye-sensitized solar cells. *nanotoday* **2017**, *14*, 42–58. [[CrossRef](#)]
6. Jiang, C.; Moniz, S.J.A.; Wang, A.; Zhang, T.; Tang, J. Photoelectrochemical devices for solar water splitting—Materials and challenges. *Chem. Soc. Rev.* **2017**, *46*, 4645–4660. [[CrossRef](#)]
7. Kim, J.H.; Lee, J.S. Solar water splitting: Elaborately modified BiVO<sub>4</sub> photoanodes for solar water splitting. *Adv. Mater.* **2019**, *31*, 1806938–1806973. [[CrossRef](#)]
8. Wang, D.; Chang, G.; Zhang, Y.; Jie, C.; Yang, J.; Shao, S.; Wang, L.; Fan, C.; Wang, L. Hierarchical three-dimensional branched hematite nanorod arrays with enhanced mid-visible light absorption for high-efficiency photoelectrochemical water splitting. *Nanoscale* **2016**, *8*, 12697–12701. [[CrossRef](#)]
9. Pang, H.; Zhao, G.; Liu, G.; Zhang, H.; Hai, X.; Wang, S.; Song, H.; Ye, J. Interfacing photosynthetic membrane protein with mesoporous WO<sub>3</sub> photoelectrode for solar water oxidation. *Small* **2018**, *14*, 1800104–1800114. [[CrossRef](#)] [[PubMed](#)]
10. Bagal, I.V.; Chodankar, N.R.; Hassan, M.A.; Waseem, A.; Johar, M.A.; Kim, D.H.; Ryu, S.W. Cu<sub>2</sub>O as an emerging photocathode for solar water splitting—A status review. *Int. J. Hydrogen Energy* **2019**, *44*, 21351–21378. [[CrossRef](#)]
11. Guo, X.; Diao, P.; Xu, D.; Huang, S.; Yang, Y.; Jin, T.; Wu, Q.; Xiang, M.; Zhang, M. CuO/Pd composite photocathodes for photoelectrochemical hydrogen evolution reaction. *Int. J. Hydrogen Energy* **2014**, *39*, 7686–7696. [[CrossRef](#)]
12. Li, C.; He, J.; Xiao, Y.; Delaunay, J.J. Earth-abundant Cu-based metal oxide photocathodes for photoelectrochemical water splitting. *Energy Environ. Sci.* **2020**, *13*, 3269–3306. [[CrossRef](#)]
13. Sharma, G.; Zhao, Z.; Sarker, P.; Nail, B.A.; Osterloh, F. Electronic structure, photovoltage, and photocatalytic hydrogen evolution with p-CuBi<sub>2</sub>O<sub>4</sub> nanocrystals. *J. Mater. Chem. A* **2016**, *4*, 2936–2942. [[CrossRef](#)]
14. Berglund, S.P.; Abdi, F.F.; Bogdanoff, P.; Chemseddine, A.; Friedrich, D.; Roel, V.D.K. Comprehensive evaluation of CuBi<sub>2</sub>O<sub>4</sub> as a photocathode material for photoelectrochemical water splitting. *Chem. Mater.* **2016**, *28*, 4231–4242. [[CrossRef](#)]
15. Hahn, N.T.; Holmberg, V.C.; Korgel, B.A.; Mullins, C.B. Electrochemical synthesis and characterization of p-CuBi<sub>2</sub>O<sub>4</sub> thin film photocathodes. *J. Phys. Chem. C* **2012**, *116*, 6459–6466. [[CrossRef](#)]
16. Cao, D.; Nasori, N.; Wang, Z.; Yan, M.; Yong, L. P-type CuBi<sub>2</sub>O<sub>4</sub>: An easily accessible photocathodic material for high-efficient water splitting. *J. Mater. Chem. A* **2016**, *4*, 8995–9001. [[CrossRef](#)]
17. Yang, J.; Du, C.; Wen, Y.; Zhang, Z.; Cho, K.; Chen, R.; Shan, B. Enhanced photoelectrochemical hydrogen evolution at p-type CuBi<sub>2</sub>O<sub>4</sub> photocathode through hypoxic calcination. *Int. J. Hydrogen Energy* **2018**, *43*, 9549–9557. [[CrossRef](#)]
18. Abdulkarem, A.M.; Li, J.; Aref, A.A.; Lu, R.; Elssfah, E.M.; Hui, W.; Ge, Y.; Ying, Y. CuBi<sub>2</sub>O<sub>4</sub> single crystal nanorods prepared by hydrothermal method: Growth mechanism and optical properties. *Mater. Res. Bull.* **2011**, *46*, 1443–1450. [[CrossRef](#)]
19. Wang, F.; Septina, W.; Chemseddine, A.; Abdi, F.F.; Friedrich, D.; Bogdanoff, P.; Krol, R.V.D.; Tilley, D.; Berglund, S.P. Gradient self-doped CuBi<sub>2</sub>O<sub>4</sub> with highly improved charge separation efficiency. *J. Am. Chem. Soc.* **2017**, *139*, 15094–15103. [[CrossRef](#)]
20. Kang, D.; Hill, J.C.; Park, Y.; Choi, K.S. Photoelectrochemical properties and photostabilities of high surface area CuBi<sub>2</sub>O<sub>4</sub> and Ag-doped CuBi<sub>2</sub>O<sub>4</sub> photocathodes. *J. High Energy Phys.* **2016**, *28*, 4331–4340. [[CrossRef](#)]
21. Oh, W.D.; Lua, S.K.; Dong, Z.; Lim, T.T. A novel three-dimensional spherical CuBi<sub>2</sub>O<sub>4</sub> consisting of nanocolumn arrays with persulfate and peroxymonosulfate activation functionalities for 1H-benzotriazole removal. *Nanoscale* **2015**, *7*, 8149–8158. [[CrossRef](#)]
22. Li, J.; Griep, M.; Choi, Y.S.; Chu, D. Photoelectrochemical overall water splitting with textured CuBi<sub>2</sub>O<sub>4</sub> as a photocathode. *Chem. Commun.* **2018**, *54*, 3331–3334. [[CrossRef](#)]
23. Xu, N.; Li, F.; Gao, L.; Hu, H.; Hu, Y.; Long, X.; Ma, J.; Jin, J.N. Cu-codoped carbon nanosheet/Au/CuBi<sub>2</sub>O<sub>4</sub> photocathodes for efficient photoelectrochemical water splitting. *ACS Sustain. Chem. Eng.* **2018**, *6*, 7257–7264. [[CrossRef](#)]
24. Wang, F.; Chemseddine, A.; Abdi, F.F.; Krol, R.; Berglund, S.P. Spray pyrolysis of CuBi<sub>2</sub>O<sub>4</sub> photocathodes: Improved solution chemistry for highly homogeneous thin films. *J. Mater. Chem. A* **2017**, *5*, 12838–12847. [[CrossRef](#)]
25. Park, H.S.; Lee, C.; Reisner, E. Photoelectrochemical reduction of aqueous protons with a CuO/CuBi<sub>2</sub>O<sub>4</sub> heterojunction under visible light irradiation. *Phys. Chem. Chem. Phys.* **2014**, *16*, 22462–22465. [[CrossRef](#)]
26. Xu, Y.; Jian, J.; Li, F.; Liu, W.; Jia, L.; Wang, H. Porous CuBi<sub>2</sub>O<sub>4</sub> photocathodes with rationally engineered morphology and composition towards high-efficiency photoelectrochemical performance. *J. Mater. Chem.* **2019**, *7*, 21997–22004. [[CrossRef](#)]
27. Patil, R.; Kelkar, S.; Naphade, R.; Ogale, S. Low temperature grown CuBi<sub>2</sub>O<sub>4</sub> with flower morphology and its composite with CuO nanosheets for photoelectrochemical water splitting. *J. Mater. Chem. A* **2014**, *2*, 3661–3668. [[CrossRef](#)]
28. Yao, B.; Zhang, J.; Fan, X.; He, J.; Li, Y. surface engineering of nanomaterials for photo-electrochemical water splitting. *Small* **2019**, *15*, 1803746–1803766. [[CrossRef](#)]

29. Reddy, C.V.; Reddy, K.R.; Shetti, N.P.; Shim, J.; Aminabhavi, T.M.; Dionysiou, D.D. Hetero-nanostructured metal oxide-based hybrid photocatalysts for enhanced photoelectrochemical water splitting—A review. *Int. J. Hydrogen Energy* **2020**, *45*, 18331–18347. [[CrossRef](#)]
30. Kumar, P.S.; Sundaramurthy, J.; Subramanian, S.; Babu, V.J.; Singh, G.; Allakhverdiev, S.I.; Ramakrishna, S. Hierarchical electrospun nanofibers for energy harvesting, production and environmental remediation. *Energy Environ. Sci.* **2014**, *7*, 3192–3222. [[CrossRef](#)]
31. Joly, D.; Jung, J.W.; Kim, I.D.; Demadrille, Electrospun materials for solar energy conversion: Innovations and trends. *J. Mater. Chem. C* **2016**, *4*, 10173–10197. [[CrossRef](#)]
32. Hildebrandt, N.C.; Soldat, J.; Marschall, R. Layered perovskite nanofibers via electrospinning for overall water splitting. *Small* **2015**, *11*, 2051–2057. [[CrossRef](#)]
33. Jo, H.S.; Kim, M.W.; Joshi, B.; Samuel, E.; Yoon, H.; Swihart, M.T.; Yoon, S. Ni-core CuO-shell fibers produced by electrospinning and electroplating as efficient photocathode materials for solar water splitting. *Nanoscale* **2018**, *10*, 9720–9728. [[CrossRef](#)]
34. Hu, G.; Hu, C.; Zhu, Z.; Lei, Z.; Qiang, W.; Zhang, H.L. Construction of Au/CuO/Co<sub>3</sub>O<sub>4</sub> tri-component heterojunction nanotubes for enhanced photocatalytic oxygen evolution under visible light irradiation. *ACS Sustain. Chem. Eng.* **2018**, *6*, 8801–8808.
35. Yuan, X.; Sun, X.; Zhou, H.; Zeng, S.; Liu, D. Free-standing electrospun W-doped BiVO<sub>4</sub> porous nanotubes for the efficient photoelectrochemical water oxidation. *Front. Chem.* **2020**, *8*, 1–10. [[CrossRef](#)]
36. Zhang, Y.C.; Yang, H.; Wang, W.P.; Zhang, H.M.; Li, R.S.; Wang, X.X.; Yu, R.C. A promising supercapacitor electrode material of CuBi<sub>2</sub>O<sub>4</sub> hierarchical microspheres synthesized via a coprecipitation route. *J. Alloys Compd.* **2016**, *684*, 707–713. [[CrossRef](#)]
37. Kim, H.; Bae, S.; Jeon, D.; Ryu, J. Fully solution-processable Cu<sub>2</sub>O–BiVO<sub>4</sub> photoelectrochemical cells for bias-free solar water splitting. *Green Chem.* **2018**, *20*, 3732–3742. [[CrossRef](#)]
38. Pulipaka, S.; Boni, N.; Ummethala, G.; Meduri, P. CuO/CuBi<sub>2</sub>O<sub>4</sub> heterojunction photocathode: High stability and current densities for solar water splitting. *J. Catal.* **2020**, *387*, 17–27. [[CrossRef](#)]
39. Yu, J.; Qi, L.; Jaroniec, M. Hydrogen Production by Photocatalytic water splitting over Pt/TiO<sub>2</sub> nanosheets with exposed (001) facets. *J. Phys. Chem. C* **2010**, *114*, 13118–13125. [[CrossRef](#)]